Journal of Sound and Vibration (2001) **246**(4), 583–600
doi:10.1006/jsvi.2000.3521, available online at http://www.idealibrary.com on IDEAL®

FORCED VIBRATION AND DYNAMIC STABILITY OF A ROTATING TAPERED COMPOSITE TIMOSHENKO SHAFT: BENDING MOTIONS IN END-MILLING OPERATIONS

W. KIM

Division for Research and Education in Mechanical Engineering, Hanyang University, Seoul, 133-791, Republic of Korea

A. ARGENTO

Department of Mechanical Engineering, University of Michigan-Dearborn, Dearborn, MI 48128, U.S.A.

AND

R. A. SCOTT

Department of Mechanical Engineering, University of Michigan, Ann Arbor, MI 48109, USA

(*Received* 31 *May* 2000, *and in final form* 14 *December* 2000)

The response and stability of a high-speed extended length endmill subjected to cutting forces typical of milling operations are studied. The system is modelled as a rotating, tapered, filament-wound composite, Timoshenko shaft having clamped–free supports, and subjected to fluctuating, deflection-dependent, cutting-type end loads, including regenerative delay effects. External and internal viscous damping are also included in the model. The general Galerkin method is used to satisfy spatial dependence in the system equations, and the system's stability and forced response are determined using various techniques. From these, it is found that improvements of performance are possible by tapering and using composite materials.

1. INTRODUCTION

Kim *et al.* [1], developed a model for an axially tapered, composite, Timoshenko shaft which is rotating about its central axis. The structure is taken to have clamped–free supports, and the model is intended to represent an extended-length endmill (i.e., a part between the tool holder and the cutter) in an end-milling operation or a boring bar in a boring operation. Free vibration and static stiffness were treated by Kim *et al.* [1]. Studies were performed which showed the advantages of cross-section tapering and the incorporation of fiber-reinforced polymeric materials on natural frequencies and static stiffness.

An important measure of an endmill design is its response and stability in a cutting operation. To this end, the model developed by Kim *et al.* [1] is extended in the present work to include milling cutting forces of the type used by Tlusty and MacNeil [2] and Smith and Tlusty [3]. These forces vary as the tool vibrates and so produce periodically

0022-460X/01/390583 + 18 $35.00/0

varying coefficients and delay terms (regenerative effects) in the differential equations of motion. Additionally, periodic forcing terms arise, as well as terms that can induce flutter-like instabilities (by which is meant the real parts of certain eigenvalues being positive). The result is a model of a system capable of forced resonance and unstable response due to regenerative effects, parametric resonance, and flutter. The model is a continuous mass distribution Timoshenko beam model including various anisotropic coupling effects. It also includes gyroscopic effects due to high rotational speed. The extraction of stability zones for such a model incorporating regenerative cutting forces has not, to the authors' knowledge, been previously reported.

The general Galerkin method is used to satisfy spatial dependence in the partial differential equations of motion and produce a set of coupled ordinary differential-delay equations, with time-dependent coefficients. From these, cutting stability diagrams and forced response during a cutting process are determined using various techniques. When the delay terms are discarded, the monodromy matrix technique is used to obtain flutter and parametric resonance zones. When the delay terms are included, a simplified approach based on the work of Altintas and Budak [4] and direct numerical integration are used to assess system stability. End-milling results are given for three design cases: non-tapered steel, non-tapered steel/composite hybrid, tapered steel/composite hybrid (results for boring operations are planned for a future work). It is shown that cutting stability is improved by the use of composites, as well as by tapering. Also, use of composites and shaft tapering, with the attendant increase in bending natural frequencies, can be beneficial from a forced motion viewpoint.

2. EQUATIONS OF MOTION

Consider the tapered, filament-wound composite shaft shown in Figure 1. The equations of motion of a uniformly rotating, tapered, filament-wound composite Timoshenko beam were derived by Kim *et al.* [1]. In the model developed, the bending motions are decoupled from the axial and torsional motions and are described by the following equations:

$$m\ddot{u}_x + \underline{(c_e + c_i)\dot{u}_x} + \underline{c_i \Omega u_y} - \{\kappa K_V^s (u_x' - \psi_x)\}' - \{\kappa K_V^o (u_y' + \psi_y)\}'$$
$$+ \{K_{VM}^s \psi_x'\}' + \{K_{VM}^o \psi_y'\}' - f_x = 0, \tag{1}$$

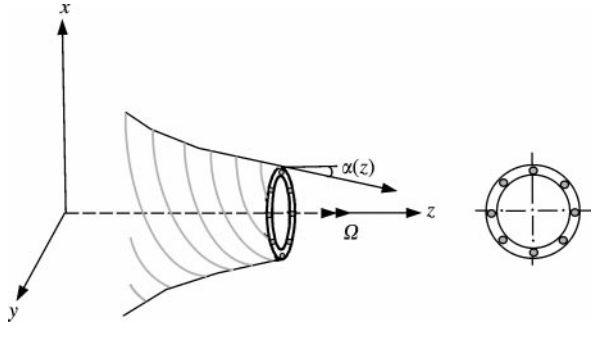

Figure 1. Single lamina of a tapered, filament-wound composite shaft.

$$m\ddot{u}_y + \underline{(c_e + c_i)\dot{u}_y} - \underline{c_i \Omega u_x} - \{\kappa K_V^s(u_y' + \psi_y)\}' + \{\kappa K_V^o(u_x' - \psi_x)\}'$$

$$- \{K_{VM}^s \psi_y'\}' + \{K_{VM}^o \psi_x'\}' - f_y = 0, \tag{2}$$

$$I_y \ddot{\psi}_x - I_z \Omega \dot{\psi}_y - \{K_M \psi_x'\}' + \{\kappa K_{MV}^s(u_x' - \psi_x)\}' + \{\kappa K_{MV}^o(u_y' + \psi_y)\}'$$

$$- \kappa K_V^s(u_x' - \psi_x) - \kappa K_V^o(u_y' + \psi_y) + K_{VM}^s \psi_x' + K_{VM}^o \psi_y' = 0, \tag{3}$$

$$I_x \ddot{\psi}_y + I_z \Omega \dot{\psi}_x - \{K_M \psi_y'\}' - \{\kappa K_{MV}^s(u_y' + \psi_y)\}' + \{\kappa K_{MV}^o(u_x' - \psi_x)\}'$$

$$+ \kappa K_V^s(u_y' + \psi_y) - \kappa K_V^o(u_x' - \psi_x) + K_{VM}^s \psi_y' - K_{VM}^o \psi_x' = 0. \tag{4}$$

Results for axial and torsional motions (as well as some static strength analyses) are given in reference [5].

Here the shaft has been taken to be rotating at a uniform rate Ω about the inertial z-axis. u_x and u_y are lateral deflections of the neutral axis, ψ_x and ψ_y are bending rotation angles about the inertial y- and x-axis, respectively, m is the mass per unit length and the I's are mass moments of inertia per unit length. The prime and overdot denote differentiation w.r.t. z and time (t) respectively. K_V^s, K_V^o, K_{VM}^s, K_{MV}^o K_{MV}^s, K_{VM}^o, and K_M are physical constants which are complicated functions involving the geometry, taper angle α, material properties of the layers and fiber angles. Details on them will not be repeated here. κ is a Timoshenko shear coefficient and f_x and f_y are applied forces per unit length in the x and y directions respectively.

Damping plays an important role in the suppression/enhancement of instabilities. Three commonly used models in rotating system dynamics are external viscous damping [6, 7], internal viscous damping [6–8] and hysteretic damping [6, 8]. External viscous damping is always stabilizing, hysteretic damping is always destabilizing (independent of rotational speed) and internal viscous damping may be destabilizing (depending on the rotational speed).

Inclusion of hysteretic damping could be achieved by using constitutive relations for linear viscoelastic solids. However, this leads to considerably increased complexity of an already complicated theoretical model and will not be pursued in this work. Note that based on work on an isotropic, Timoshenko shaft [8] it can be concluded that hysteretic damping plays a minor role compared to viscous damping for clamped–free boundary conditions.

For composite shafts the damping scenario is far more complex [9] and depends on multiple loss factors (anisotropic damping) related to the specific lay-up of the structure (see e.g., references [10, 11]). In spite of the complexity, recent tests have been conducted on spinning composite rotors [12] that show, like isotropic rotors, the damping effect decreases with increase in rotational speed, but the rotors are stable up to the critical speed.

In light of the above, it might be expected that even for a stable response, hysteretic damping would effectively result in reduced overall damping in the rotating system. To account for this in the present work conservative estimates of the viscous damping coefficient values will be used.

Damping terms were not included in Kim *et al.* [1]. These additional terms are underlined in equations (1) and (2); c_e is an external viscous damping constant per unit length and c_i is an internal viscous damping constant per unit length. c_e is proportional to the speed in the inertial co-ordinate system and c_i is proportional to the speed in the rotating co-ordinate system [6–8].

The shaft is taken to be fixed at $z = 0$ and free at $z = L$, so that the boundary conditions are

$$u_x(0) = u_y(0) = \psi_x(0) = \psi_y(0) = 0, \tag{5}$$

$$\kappa(L)K_V^s(L)\{u_x'(L) - \psi_x(L)\} + \kappa(L)K_V^o(L)\{u_y'(L) + \psi_y(L)\} - K_{VM}^s(L)\psi_x'(L) - K_{VM}^o(L)\psi_y'(L) = 0, \tag{6}$$

$$\kappa(L)K_V^s(L)\{u_y'(L) + \psi_y(L)\} - \kappa(L)K_V^o(L)\{u_x'(L) - \psi_x(L)\} + K_{VM}^s(L)\psi_y'(L) - K_{VM}^o(L)\psi_x'(L) = 0, \tag{7}$$

$$K_M(L)\psi_x'(L) - \kappa(L)K_{MV}^s(L)\{u_x'(L) - \psi_x(L)\} - \kappa(L)K_{MV}^o(L)\{u_y'(L) + \psi_y(L)\} = 0, \tag{8}$$

$$K_M(L)\psi_y'(L) + \kappa(L)K_{MV}^s(L)\{u_y'(L) + \psi_y(L)\} - \kappa(L)K_{MV}^o(L)\{u_x'(L) - \psi_x(L)\} = 0. \tag{9}$$

3. GALERKIN METHOD

Analytic solutions to equations (1)–(4) are not feasible and here the Galerkin method is used. One takes

$$u_x = \sum_{n=1}^{N_G} A_n^{(x)}(t)\xi_n(z), \qquad u_y = \sum_{n=1}^{N_G} A_n^{(y)}(t)\xi_n(z), \tag{10, 11}$$

$$\psi_x = \sum_{n=1}^{N_G} B_n^{(x)}(t)\alpha_n(z), \qquad \psi_y = \sum_{n=1}^{N_G} B_n^{(y)}(t)\alpha_n(z). \tag{12, 13}$$

The Galerkin functions ξ_n for the variables u_x and u_y are taken to be the mode shapes of a uniform, non-rotating, isotropic, fixed–free Euler–Bernoulli beam. The Galerkin functions α_n for the angular deformations ψ_x and ψ_y are taken to be

$$\alpha_n = \sin\frac{(2n-1)\pi z}{2L}. \tag{14}$$

The Galerkin functions used do not satisfy the boundary conditions (6)–(9). Hence the so-called general Galerkin method is used (see references [13, 1]). The procedure yields a set of equations of the form

$$[M]\begin{Bmatrix}\{\ddot{A}_n^{(x)}\}\\ \{\ddot{A}_n^{(y)}\}\\ \{\ddot{B}_n^{(x)}\}\\ \{\ddot{B}_n^{(y)}\}\end{Bmatrix} + [G]\begin{Bmatrix}\{\dot{A}_n^{(x)}\}\\ \{\dot{A}_n^{(y)}\}\\ \{\dot{B}_n^{(x)}\}\\ \{\dot{B}_n^{(y)}\}\end{Bmatrix} + [K]\begin{Bmatrix}\{A_n^{(x)}\}\\ \{A_n^{(y)}\}\\ \{B_n^{(x)}\}\\ \{B_n^{(y)}\}\end{Bmatrix} = \{F\}, \tag{15}$$

where, e.g.,

$$M_{11} = \int_0^L m\xi_1\xi_1\,\mathrm{d}z, \qquad G_{11} = \int_0^L (c_e + c_i)\xi_1\xi_1\,\mathrm{d}z, \qquad K_{11} = \int_0^L \kappa K_V^s\xi_1'\xi_1'\,\mathrm{d}z. \tag{16–18}$$

These coefficients are calculated numerically (with the aid of MAPLE [14]). Also

$$\{F\} = \begin{Bmatrix} \{f_n^{(x)}\} \\ \{f_n^{(y)}\} \\ \{0\} \\ \{0\} \end{Bmatrix}, \tag{19}$$

where

$$f_n^{(x)} = \int_0^L f_x \xi_n \, \mathrm{d}z, \qquad f_n^{(y)} = \int_0^L f_y \xi_n \, \mathrm{d}z. \tag{20, 21}$$

The free vibration problem, $\{F\} = \{0\}$, has been treated by Kim *et al.* [1]. Here attention is focused on the case $\{F\} \neq \{0\}$.

4. CUTTING FORCE MODEL

Consider a half immersion, up-milling operation with a four-fluted, end-milling cutter (see Figure 2). Here, only a steady state end-milling operation is treated and the workpiece is assumed to be rigid. A deflection-dependent cutting force model is used. The tangential and radial forces are based on the work of Tlusty and MacNeil [2] and Smith and Tlusty [3].

It turns out that in the subsequent work on stability the cutting force modelling plays a significant role and some elaboration on it is appropriate. Shown in Figure 3 are sketches of the cut surface corresponding to one cutting tooth passing. For clarity, the figure depicts a moving tool in the horizontal direction, instead of a moving workpiece. θ_t denotes the angular position of the engaged tooth ($0 \leqslant \theta_t < 0{\cdot}5\pi$) and O_1, O_2 are the positions of the shaft center at time $t - T$ and t, respectively, T being the tooth period ($T = 2\pi/(N_t\Omega)$ where the number of teeth is $N_t = 4$).

The wavy lines depict the cut surfaces at times $t - T$ and t. If there were no vibrations, these surfaces would be circular and the chip thickness would be P_1P_2. Due to the vibration the actual chip thickness is $P_1P_2 - u_r(t) + u_r(t - T')$ where u_r is the deflection of the cutter

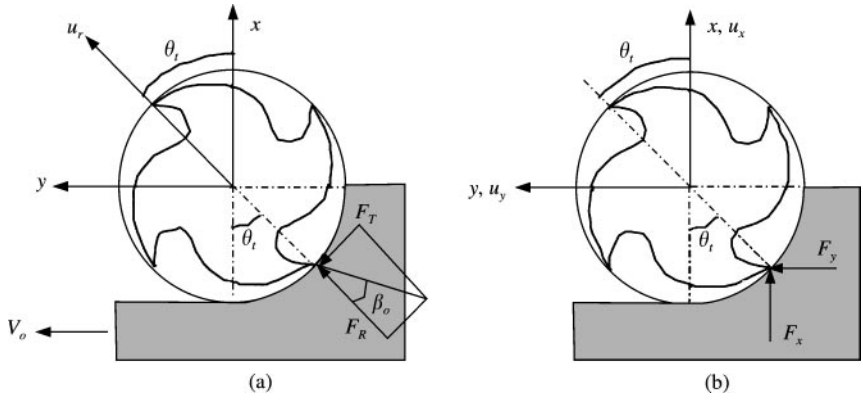

Figure 2. Cutting force model: (a) tangential and radial cutting forces, (b) transformed cutting forces along the x- and y-axis.

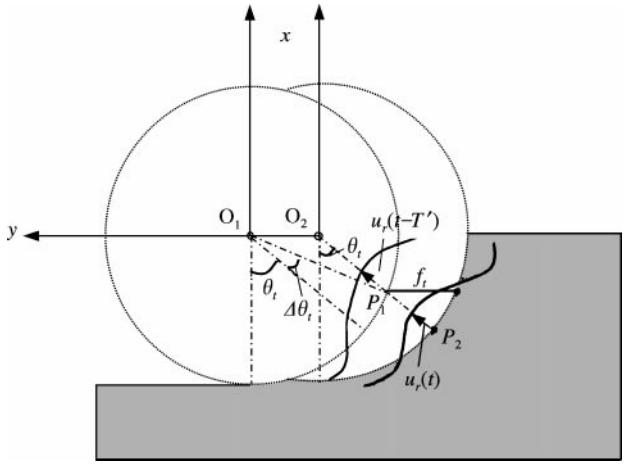

Figure 3. Sketches of the cut surface (not drawn to scale).

normal to the cut surface (without the undulations), $T' = T - \Delta T$ and $\Delta T = \Delta\theta_t/\Omega$. If $\Delta\theta_t$ is small (as it is in practice), T' can be replaced by T. Also, the approximation $P_1P_2 = f_t \sin\theta_t$ is used where f_t is the feed per tooth. In the works of Tlusty and MacNeil [2] and Smith and Tlusty [3] the tangential cutting force is taken to be proportional to the chip thickness. This together with the above approximations leads to

$$F_T(t) = K_s d\,[f_t \sin\theta_t - u_r(t) + u_r(t - T)], \tag{22}$$

where K_s is the specific cutting force per unit chip area and d is the axial depth of cut (width of chip in the z direction). The value of K_s (551·6 MPa) is obtained from Tlusty [15] for milling of aluminum. Note that if there is no loss of contact between the tooth and the workpiece, terms of the form $u_r(t - 2T), u_r(t - 3T), \ldots,$ do not enter into the picture. The inclusion of the delay term $u_r(t - T)$ is known as "the regenerative effect".

In the model, the radial cutting forces are taken to be given by

$$F_R(t) = \frac{F_T(t)}{\tan\beta_o}, \tag{23}$$

where β_o (= 73·3°) [2] is the constant angle between the normal to the cut surface (without the undulations) and the direction of the cutting force. The variation of θ_t along the z (axial) direction due to the helix angle of an end-milling cutter is neglected because the axial depth of cut, d, in the cases simulated in the study is small. Note that if the deflection of the cutter is very large, F_T as given by equation (22) can become negative; the tooth can temporarily lose contact with the workpiece. When this condition occurs, the cutting forces are set to zero in the direct numerical simulation. When F_T becomes positive again, the cutting forces are reactivated.

From Figure 2, cutting forces along the x- and y-axis are obtained by a co-ordinate transformation, giving

$$F_x(t) = F_{x0}(t) - F_{x1}(t)\{u_x(t) - u_x(t - T)\} - F_{x2}(t)\{u_y(t) - u_y(t - T)\}, \tag{24}$$

$$F_y(t) = F_{y0}(t) - F_{y1}(t)\{u_x(t) - u_x(t - T)\} - F_{y2}(t)\{u_y(t) - u_y(t - T)\}, \tag{25}$$

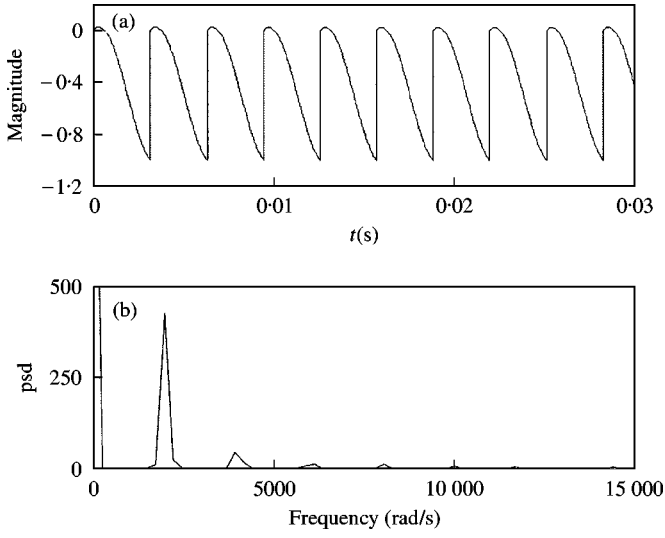

Figure 4. Plots of the periodic coefficient $F_{x2}(t)/(K_s d)$ when $\Omega = 500$ rad/s: (a) magnitude versus time, (b) power spectral density.

where

$$F_{x0}(t) = \frac{K_s d f_t}{2}\left\{-1 + \frac{1}{\sin\beta_o}\sin(2\theta_t + \beta_o)\right\}, \tag{26}$$

$$F_{x1}(t) = \frac{K_s d}{2}\left\{\frac{1}{\tan\beta_o} + \frac{1}{\sin\beta_o}\cos(2\theta_t + \beta_o)\right\}, \tag{27}$$

$$F_{x2}(t) = \frac{K_s d}{2}\left\{-1 + \frac{1}{\sin\beta_o}\sin(2\theta_t + \beta_o)\right\}, \tag{28}$$

$$F_{y0}(t) = \frac{K_s d f_t}{2}\left\{\frac{1}{\tan\beta_o} - \frac{1}{\sin\beta_o}\cos(2\theta_t + \beta_o)\right\}, \tag{29}$$

$$F_{y1}(t) = \frac{K_s d}{2}\left\{1 + \frac{1}{\sin\beta_o}\sin(2\theta_t + \beta_o)\right\}, \tag{30}$$

$$F_{y2}(t) = \frac{K_s d}{2}\left\{\frac{1}{\tan\beta_o} - \frac{1}{\sin\beta_o}\cos(2\theta_t + \beta_o)\right\}, \tag{31}$$

$$\theta_t = \text{remainder of}\left(\frac{\Omega t}{0{\cdot}5\pi}\right) = \begin{cases} \Omega t, & \text{if } 0 \leqslant \Omega t < 0{\cdot}5\pi, \\ \Omega t - 0{\cdot}5\pi, & \text{if } 0{\cdot}5\pi \leqslant \Omega t < \pi, \\ \vdots & \vdots \end{cases} \tag{32}$$

Note that these forces are deflection dependent and involve delay terms and periodic coefficients. To illustrate the periodicity, a plot of $F_{x2}(t)/(K_s d)$ versus time when $\Omega = 500$ rad/s is shown in Figure 4(a) and its power spectral density (psd) is given in Figure 4(b).

The cutting forces are treated as concentrated loads at $z = L$. Then f_x and f_y in equations (20) and (21) are given by (δ denotes a Dirac-delta function)

$$f_x = F_x(t)\delta(z - L), \qquad f_y = F_y(t)\delta(z - L). \tag{33, 34}$$

Thus, equations (15), (24) and (25) lead to a set of non-homogenous, coupled ordinary differential-delay equations of the form

$$[M]\{\ddot{Z}(t)\} + [G]\{\dot{Z}(t)\} + [K]\{Z(t)\} + ([K_f] + [K_p(t)])\{\{Z(t)\} - \{Z(t-T)\}\} = \begin{Bmatrix} \{f_{0n}^{(x)}\} \\ \{f_{0n}^{(y)}\} \\ \{0\} \\ \{0\} \end{Bmatrix}, \tag{35}$$

where

$$\{Z(t)\} = \begin{Bmatrix} [A_n^{(x)}(t)\} \\ \{A_n^{(y)}(t)\} \\ \{B_n^{(x)}(t)\} \\ \{B_n^{(y)}(t)\} \end{Bmatrix}, \qquad [K_f] = \frac{K_s d}{2} \begin{bmatrix} \dfrac{1}{\tan\beta_o}[Z_{mn}] & -[Z_{mn}] & [0] & [0] \\ [Z_{mn}] & \dfrac{1}{\tan\beta_o}[Z_{mn}] & [0] & [0] \\ [0] & [0] & [0] & [0] \\ [0] & [0] & [0] & [0] \end{bmatrix}, \tag{36, 37}$$

$$[K_p(t)] = \frac{K_s d}{2\sin\beta_o} \begin{bmatrix} \cos(2\theta_t + \beta_o)[Z_{mn}] & \sin(2\theta_t + \beta_o)[Z_{mn}] & [0] & [0] \\ \sin(2\theta_t + \beta_o)[Z_{mn}] & -\cos(2\theta_t + \beta_o)[Z_{mn}] & [0] & [0] \\ [0] & [0] & [0] & [0] \\ [0] & [0] & [0] & [0] \end{bmatrix}, \tag{38}$$

$$\{f_{0n}^{(x)}\} = F_{x0}\{\xi_n(L)\}, \qquad \{f_{0n}^{(y)}\} = F_{y0}\{\xi_n(L)\}, \qquad Z_{mn} = \xi_m(L)\xi_n(L). \tag{39–41}$$

Note that the system contains a traditional stiffness matrix $[K]$, as well as two additional matrices $[K_f]$ and $[K_p(t)]$ which are due to the deflection-dependent force. The off-diagonal terms in $[K_f]$ are of opposite signs and can cause flutter-like instabilities. The elements of $[K_p(t)]$ are periodic in time and so can give rise to parametric instabilities. Also, note that there will be effects due to the time-delay terms ($Z(t - T)$).

5. STABILITY

Consider instabilities due to the homogeneous equations [zero right-hand side in equation (35)]. Extraction of numerical results from equation (35) presents some formidable difficulties due to the presence of the time-dependent coefficients and the delay terms. Without the delay terms, parametric and flutter instabilities can be, and were, found using monodromy matrix techniques (a brief description of which is given in Appendix A). Incorporation of delay terms has been treated by Minis and Yanushevsky [16], using an analytic Fourier series approach. The method is complicated and a simple method developed by Altintas and Budak [4] for a lumped mass model is adopted here for

generating most of the results. The essence of their approach is that the time-dependent coefficients are expanded in a Fourier series, retaining only a few terms. They in fact showed that retention of only the constant term is usually adequate for prediction of stability in milling (this has been verified in the present research). The application of their procedure to the continuous composite beam model will now be given. Expanding $[K_p(t)]$ in a Fourier series (period T) and retaining only the constant term, the homogenous version of equation (35) becomes

$$[M]\{\ddot{Z}(t)\} + [G]\{\dot{Z}(t)\} + [K]\{Z(t)\} + \frac{K_s d}{2}[A_0]\{\{Z(t)\} - \{Z(t-T)\}\} = \{0\}, \quad (42)$$

where

$$[A_0] = \begin{bmatrix} \left(\frac{1}{\tan\beta_o} - \frac{2}{\pi}\right)[Z_{mn}] & \left(-1 + \frac{2}{\pi\tan\beta_o}\right)[Z_{mn}] & [0] & [0] \\ \left(1 + \frac{2}{\pi\tan\beta_o}\right)[Z_{mn}] & \left(\frac{1}{\tan\beta_o} + \frac{2}{\pi}\right)[Z_{mn}] & [0] & [0] \\ [0] & [0] & [0] & [0] \\ [0] & [0] & [0] & [0] \end{bmatrix}. \quad (43)$$

The solution to equation (42) is sought in the form

$$\{Z(t)\} = \{Z_0\}e^{i\omega t}, \qquad \{Z(t-T)\} = \{Z_0\}e^{i\omega(t-T)}. \quad (44, 45)$$

Substitution of equations (44) and (45) into equation (42) shows that for non-trivial solutions one must have

$$\det([K] - \omega^2[M] + i\omega[G] + \tfrac{1}{2}K_s d(1 - e^{-i\omega T})[A_0]) = 0. \quad (46)$$

Equation (46) is a highly non-linear (due to the $e^{-i\omega T}$ term) transcendental equation and extraction of the roots ω, which are in general complex ($\omega = \omega_R + i\omega_I$), is quite difficult. If $\omega_I > 0 (< 0)$, the motions are stable (unstable). Thus, the stability boundaries in d versus Ω space are found by setting $\omega_I = 0$ and $\omega_R = \omega_c$ ("chatter" frequency). Then equation (46) becomes

$$\det([K] - \omega_c^2[M] + i\omega_c[G] + \lambda[A_0]) = 0, \quad (47)$$

where

$$\lambda = \tfrac{1}{2}K_s d_{lim}(1 - e^{-i\omega_c T}) = \tfrac{1}{2}K_s d_{lim}(1 - \cos\omega_c T + i\sin\omega_c T). \quad (48)$$

In equation (48), d_{lim} denotes the value of d on the stability boundary. For a given ω_c, equation (47) gives a set of complex eigenvalues,

$$\lambda^{(n)} = \lambda_R^{(n)} + i\lambda_I^{(n)}, \quad n = 1, 2, \ldots, \quad (49)$$

and from equations (48) and (49) one obtains

$$d_{lim}^{(n)} = \frac{2\lambda_R^{(n)}}{K_s(1 - \cos\omega_c T)} = \frac{2\lambda_I^{(n)}}{K_s \sin\omega_c T}. \quad (50)$$

$\kappa^{(n)}$ is defined from equation (50) as

$$\kappa^{(n)} \equiv \frac{\lambda_I^{(n)}}{\lambda_R^{(n)}} = \frac{\sin \omega_c T}{1 - \cos \omega_c T}. \tag{51}$$

From equation (51)

$$\omega_c T = \cos^{-1} \frac{(\kappa^{(n)})^2 - 1}{(\kappa^{(n)})^2 + 1} \equiv \varepsilon + 2k\pi, \quad k = 0, 1, 2 \ldots. \tag{52}$$

By substituting equation (52) into equation (50) one can finally obtain

$$d_{lim}^{(n)} = \frac{\lambda_R^{(n)}}{K_s}(1 + (\kappa^{(n)})^2). \tag{53}$$

Note that the axial depth of cut (d_{lim}) should have a positive value.

The numerical procedure is as follows.

(1) Select k (each k will give a different lobe).
(2) Assume a (real) value of ω_c (guided by the system natural frequencies).
(3) Assume a phase angle ε ($0 \leqslant \varepsilon < 2\pi$).
(4) Calculate a period T from equation (52) and then calculate a rotational speed.

$$\Omega = \frac{2\pi}{N_t T}.$$

(5) Solve equation (47) for the λ's and check to see if equation (51) is satisfied. If several λ's satisfy equation(51), choose the λ leading to the smallest axial depth of cut, as determined from equation (53). If none of the λ's satisfy equation (51), increase the value of ε and proceed until it is satisfied.
(6) Repeat the procedure for new ω_c's, until a complete stability lobe has been obtained.
(7) Repeat the procedure for new k's, to obtain other stability lobes.

Direct numerical simulation (hereafter denoted as DNS) of the differential-delay equation (35) is also possible using Simulink [17]. A study was undertaken to determine the accuracy of the approximation versus DNS. The configuration treated is a tapered steel/composite hybrid shaft as shown in Figure 5(a). The stacking sequence is steel / $[85/(\pm 3)_2/-85/(\pm 3)_2]_2/85/(\pm 3)_2$ and the composite materials used in this study are high-modulus carbon/epoxy for $\pm 3^\circ$ layers [density = 1732 kg/m^3 (given by the rule of mixtures when the volume fraction of the fiber is 55%), $E_1 = 435$ GPa, $E_2 = 9$ GPa, $G_{12} = 3{\cdot}1$ GPa, $G_{23} = 3{\cdot}2$ GPa, $\nu_{12} = 0{\cdot}31$, $\nu_{23} = 0{\cdot}39$] and glass/epoxy for $\pm 85^\circ$ layers [density = 1980 kg/m^3 (given by the rule of mixtures when the volume fraction of the fiber is 60%), $E_1 = 54$ GPa, $E_2 = 16$ GPa, $G_{12} = 7$ GPa, $G_{23} = 6$ GPa, $\nu_{12} = 0{\cdot}25$, $\nu_{23} = 0{\cdot}32$]. The Timoshenko shear coefficient is treated in the same manner as in Kim *et al.* [1], the details of which will not be reproduced here. Damping values were assigned based on concepts from a single-degree-of-freedom oscillator, namely

$$(c_e + c_i) = \frac{2\varsigma\omega_1 M_{11}}{\int_0^L (\xi_1)^2 \, dz}, \tag{54}$$

where ς is the damping ratio and ω_1 is the lowest natural bending frequency at $\Omega = 0$. Picking a (small) ς value, equation (54) gives the $(c_e + c_i)$ value used. The "reasonableness"

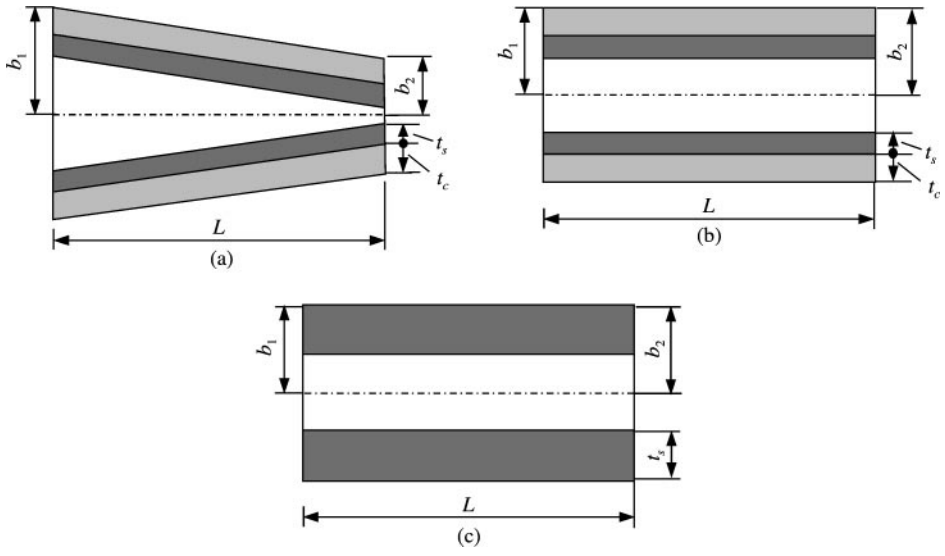

Figure 5. Simulation cases (not drawn to scale): (a) tapered composite shaft with steel core, mass = 339 g, $L = 133$ mm, $t_c = 6{\cdot}35$ mm, $t_s = 4{\cdot}7625$ mm, $b_1 = 18{\cdot}6375$ mm, $b_2 = 13{\cdot}1125$ mm; (b) non-tapered composite shaft with steel core, mass = 339 g, $L = 133$ mm, $t_c = 6{\cdot}35$ mm, $t_s = 4{\cdot}7625$ mm, $b_1 = b_2 = 15{\cdot}875$ mm; (c) non-tapered hollow steel shaft, mass = 738 g, $L = 133$ mm, $t_s = 11{\cdot}1125$ mm, $b_1 = b_2 = 15{\cdot}875$ mm.

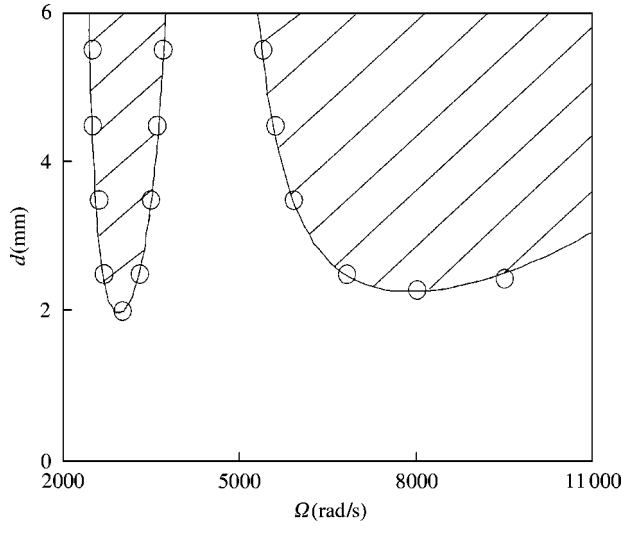

Figure 6. Stability lobes of the tapered steel/composite hybrid shaft ($c_i/(c_e + c_i) = 0{\cdot}5$, hatched regions are unstable): ——, analytical method (Altintas and Budak [4]); ○, DNS.

of this value of $(c_e + c_i)$ was checked by inspecting the decay rate in a numerically obtained solution to an initial value problem. For the problem at hand ς was taken to be 0·01 and 0·015 for steel and steel/composite hybrid, respectively. As stated earlier in the general discussion on damping, these values are on the conservative side. Use of two Galerkin functions was found to be adequate for convergence. Shown in Figure 6 are plots of stability lobes in d (axial depth of cut)–Ω (rotational speed) space by the analytical method based on

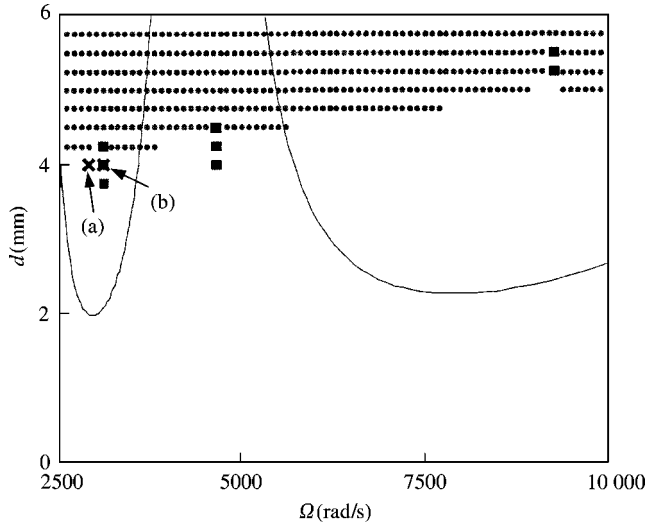

Figure 7. Stability plots of the tapered steel/composite hybrid shaft ($c_i/(c_e + c_i) = 0{\cdot}5$): ——, DNS; ·····, monodromy matrix technique (flutter); ■, monodromy matrix technique (parametric resonance).

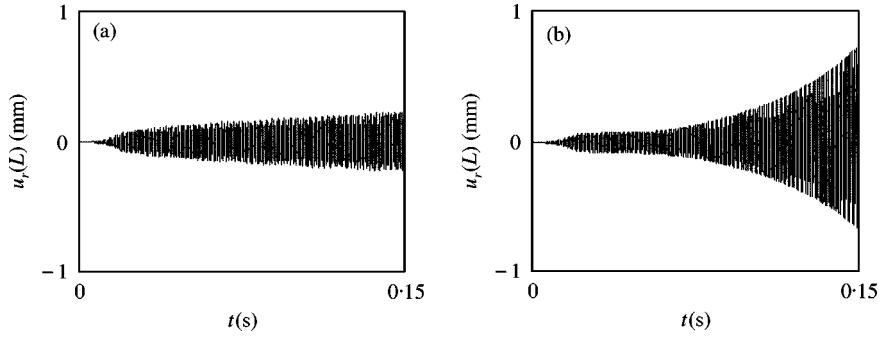

Figure 8. Response of the tapered steel/composite hybrid shaft: (a) cutting conditions outside the parametric resonance zone, (b) cutting conditions within the parametric resonance zone.

the work of Altintas and Budak [4] and DNS. There c_i was taken to be equal to c_e [with the actual numerical values being computed from equation (54)]. Excellent agreement is seen. From this perspective, retention of only the constant term in the Fourier expansion is fully adequate to describe the instabilities due to delay. Another issue though is what happens to the flutter and parametric instabilities (the latter cannot be found using the one term Fourier approximation). Shown in Figure 7 are plots of flutter and parametric instabilities obtained using the monodromy matrix technique (no delay) and the results of DNS. Several important observations can be made. Some of the parametric resonance zones lie in the delay instability zones and some have disappeared. Thus, the dominant instability mechanism is due to the delay term. An interesting point to note is that although here the two parametric resonance zones lie within the delay instability region, they do have a pronounced effect on the rate of response growth. Figure 8 shows this for cutting conditions of point (a)—outside the parametric instability zone—and point (b)—inside the parametric instability zone—labelled in Figure 7 [additional nearby points outside the

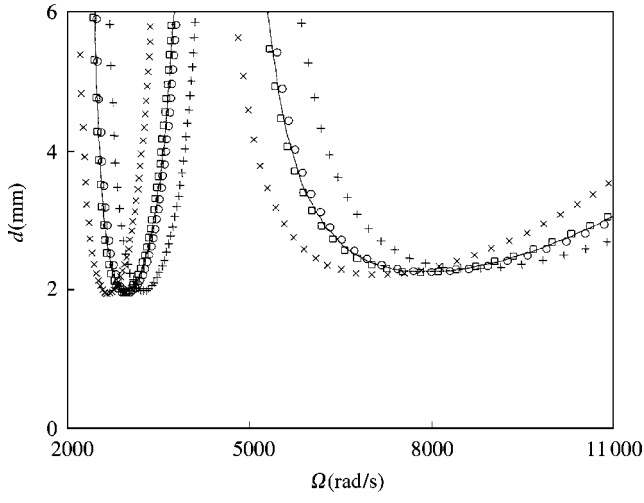

Figure 9. Effects of small changes in the amount of delay, T: ——, T; ○, 1·01 T; □, 0·99 T; +, 1·1T; ×, 0·9T.

parametric resonance zone were tested and found to behave like point (a)]. Regarding flutter, a portion of the flutter boundary has disappeared and the remaining portion lies within the delay instability boundaries. Again the dominant player is the delay term.

In deriving equation (22) some approximations were made, as a consequence of which the delay might not be exactly T, so an issue is how robust the above results are. Shown in Figure 9 are results for several other values of delay, obtained using the one-term Fourier approximation. It is seen that the instability boundaries are insensitive to small changes in the amount of delay.

Figure 10 shows how the instability zones change with the values of internal and external viscous damping, for the tapered steel/composite hybrid shaft. Figure 10(a) is a plot for $c_i/(c_e + c_i) = 0$, i.e., no internal damping, and Figure 10(b) is a plot for $c_i/(c_e + c_i) = 0{\cdot}5$, i.e., internal damping value is the same as external damping value keeping $\varsigma = 0{\cdot}015$. Note that due to the destabilizing effect of internal damping a new instability zone appears at high rotational speeds in Figure 10(b). Increasing the ratio of internal damping $[c_i/(c_e + c_i)]$ up to 1·0 [see Figure 10(c)], i.e., no external damping, the instability zone due to the internal damping is increased and starts at the critical speed ($\approx 18\,500$ rad/s). These stability plots are obtained by a one-term Fourier series approximation (no time-dependent periodic coefficients in the equations of motion) and also verified by DNS (with periodic coefficients). Thus, even with inclusion of the time-dependent terms, the instabilities due to internal viscous damping still begin at the first whirling speed. Note that the destabilizing effect of internal damping can be neglected in this study because the practical operation ranges in milling are well below the critical speed.

Shown in Figure 11 are results for damping values of $\varsigma = 0{\cdot}015$ and 0·02 when $c_i/(c_e + c_i) = 0{\cdot}5$. It is seen that increasing the damping has a significant effect on the locations and widths of the chatter zones. The most significant point is that larger stable depths of cut can be employed if the damping is increased. For example, at all speeds, the stable depth of cut is seen to increase by about 30% via the higher damping value of 0·02.

In summary, it may be concluded that the method using the one-term Fourier series approximation leads to accurate and robust results on stability in end-milling. Since the method is considerably less computer intensive than DNS, it is employed next to explore

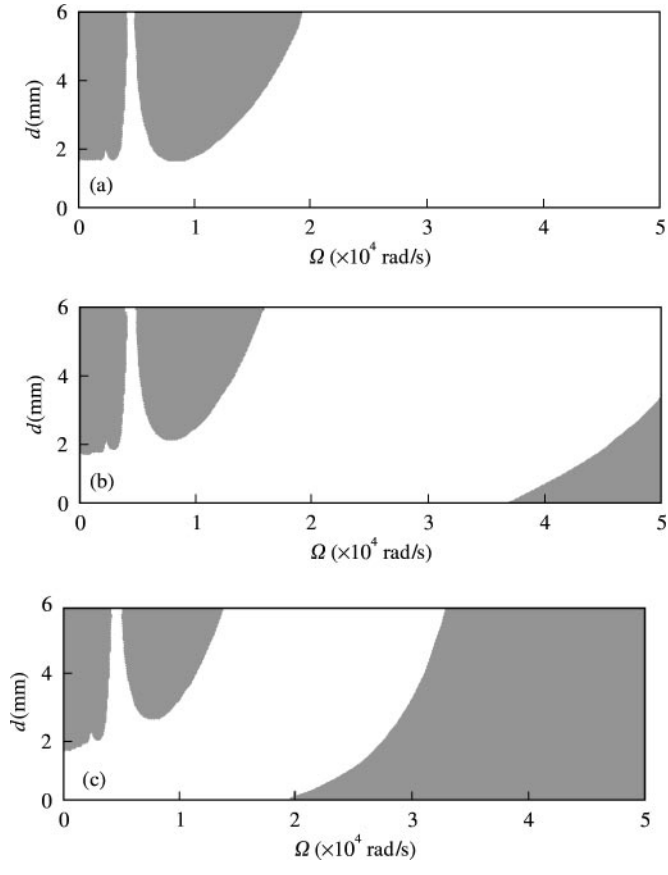

Figure 10. Effects of the external and internal damping (black regions are unstable): (a) $c_i/(c_e + c_i) = 0$, (b) $c_i/(c_e + c_i) = 0{\cdot}5$; (c); $c_i/(c_e + c_i) = 1$.

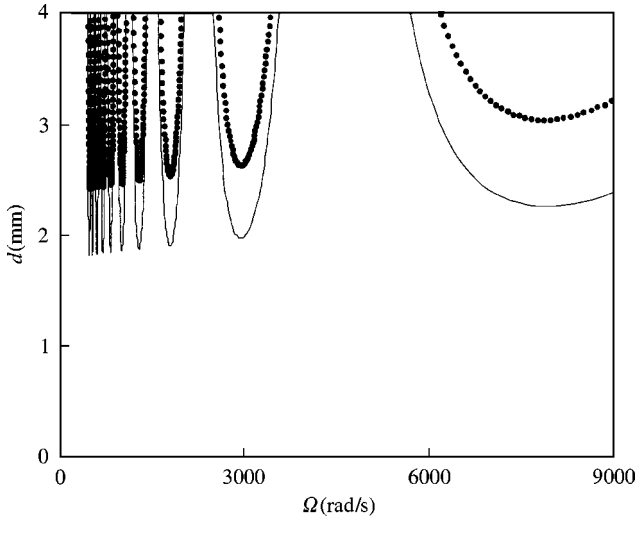

Figure 11. Effects of damping values ($c_i/(c_e + c_i) = 0{\cdot}5$): ——, $\varsigma = 0{\cdot}015$; ·····, $\varsigma = 0{\cdot}02$.

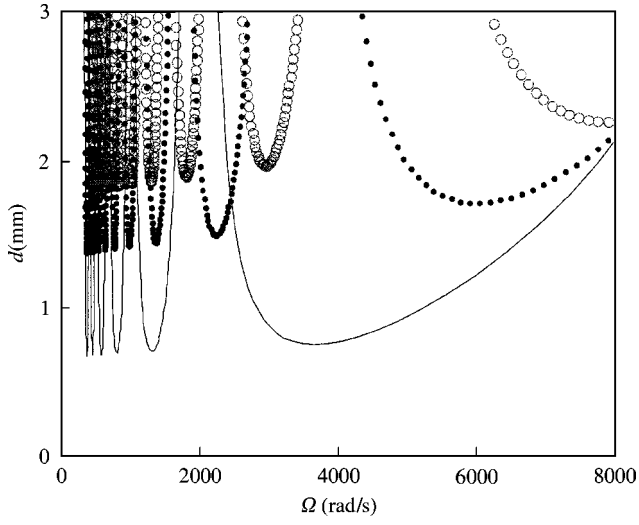

Figure 12. Stability lobes ($c_i/(c_e + c_i) = 0{\cdot}5$): ○, tapered steel/composite hybrid; ·····, non-tapered steel/composite hybrid; ——, non-tapered hollow steel.

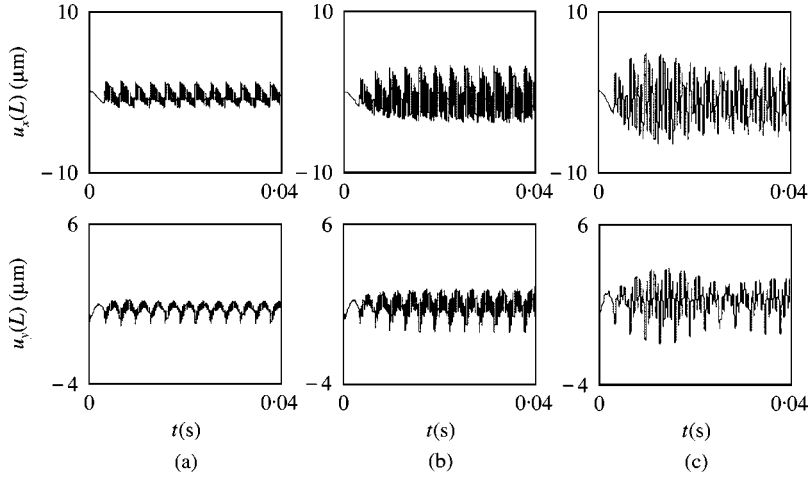

Figure 13. Deflections due to cutting forces ($\Omega = 500$ rad/s, $d = 0{\cdot}6$ mm, $f_t = 0{\cdot}1$ mm, $c_i/(c_e + c_i) = 0{\cdot}5$): (a) tapered steel/composite hybrid, (b) non-tapered steel/composite hybrid, (c) non-tapered hollow steel.

the merits of various shaft designs (Figure 5), all involving the same volumes. Shown in Figure 12 are plots of stability lobes for tapered steel/composite hybrid, non-tapered steel/composite hybrid, and non-tapered steel. The stable regions of the tapered steel/composite hybrid shaft are larger than those of the non-tapered steel/composite hybrid shaft [due to higher bending stiffness produced by shaft tapering [1]]. Also, the stable regions of the non-tapered steel/composite hybrid shaft are larger than those of the non-tapered steel shaft due to higher damping as well as higher bending stiffness.

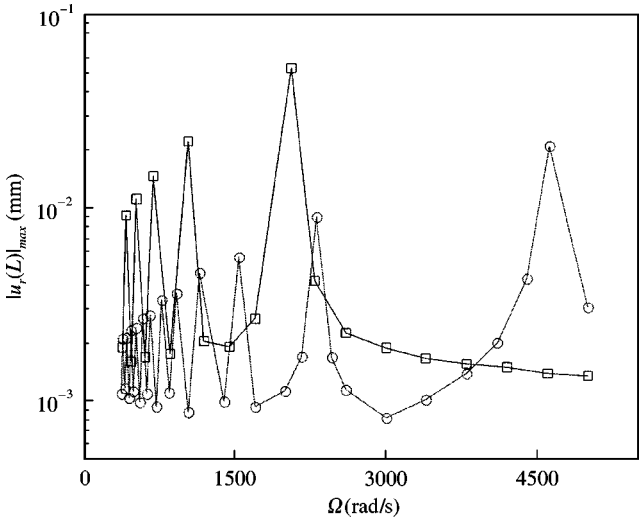

Figure 14. Maximum radial deflection at $z = L$: ○, tapered steel/composite hybrid; □, non-tapered hollow steel.

6. FORCED MOTIONS

Some effects of the non-homogeneous terms in equation (35) will now be explored via direct numerical integration. Shown in Figure 13 are plots of $u_x(L)$ and $u_y(L)$ as functions of time for $\Omega = 500$ rad/s, $d = 0{\cdot}6$ mm, $f_t = 0{\cdot}1$ mm and $c_i/(c_e + c_i) = 0{\cdot}5$. Inspection of these figures yields the maximum values of the deflection. From such data, plots of the peak value of $u_r(L)$ versus Ω can be constructed and these are shown in Figure 14 for the tapered steel/composite hybrid shaft and the non-tapered hollow steel shaft. Note that there are many forced resonance peaks because the applied force is not pure sinusoidal, as shown in Figure 4. The results show that for Ω up to 3800 rad/s use of the tapered composite material shaft is beneficial in that the values of $|u_r(L)|_{max}$ are less than those for the non-tapered steel shaft, with the exception of a region in the vicinity of $\Omega = 1500$ rad/s. However, as Ω approaches 4500 rad/s, the 4Ω component in the forcing term approaches the lowest bending natural frequency of the tapered steel/composite shaft. Resonance is being approached and the trends reverse. Thus, use of composites and shaft tapering, with the attendant increase in bending natural frequencies is beneficial, from a forced motion viewpoint, provided the operational speeds are below the first natural frequency divided by four (for a four-fluted cutter), which, in practice, is typically the case.

7. SUMMARY AND CONCLUSIONS

A continuous parameter model has been developed for a rotating, tapered, composite shaft (representing an extended length endmill), subject to fluctuating, deflection-dependent cutting-type end loads. Regenerative (delay) effects and external and internal viscous damping are included in the model.

The general Galerkin method leads to a set of ordinary differential-delay equations with time-dependent coefficients. Extraction of numerical information from such equations is a very challenging task, the system being prone to parametric, flutter-like and

regenerative-type instabilities ("chatter"). It was shown that the one-term Fourier series approximation used by Altintas and Budak [4] leads to quite accurate results as determined by comparisons with direct numerical integration, performed with the aid of Simulink. The main results were obtained using the Altintas and Budak approximation.

Several design scenarios were considered, namely tapered steel/composite hybrid, non-tapered steel/composite hybrid, and non-tapered steel shafts. In all cases treated it was found that the dominant instability mechanism was chatter. Instability zones due to internal viscous damping were also found, which even with inclusion of the time-dependent terms in the equations still begin at the first whirling speed (in the absence of external viscous damping). It was found that increasing the damping has a significant effect on the locations and widths of the chatter zones. Larger stable depths of cut can be employed if the damping is increased. The stable depth of cut increases by about 30% if the damping value is increased by 33%.

It was also found that the stable regions of the tapered steel/composite hybrid shaft are larger than those of the non-tapered steel/composite hybrid shaft. Also, the stable regions of the non-tapered steel/composite hybrid shaft are larger than those of the non-tapered steel shaft.

Finally, it was shown that use of composites and shaft tapering is beneficial, from a forced motion viewpoint, provided the operational speeds are below the first natural frequency divided by four (for a four-fluted cutter).

ACKNOWLEDGMENTS

This work was supported by U.S.A. National Science Foundation Grant Number DMI-9522897 to the second author.

REFERENCES

1. W. Kim, A. Argento and R. A. Scott 1999 *Journal of Sound and Vibration* **226**, 125–147. Free vibration of a rotating tapered composite Timoshenko shaft.
2. J. Tlusty and P. Macneil 1975 *Annals of the CIRP* **24**, 21–25. Dynamics of cutting forces in end milling.
3. S. Smith and J. Tlusty 1991 *Journal of Engineering for Industry* **113**, 169–175. An overview of modeling and simulation of the milling process.
4. Y. Altintas and E. Budak 1995 *Annals of the CIRP* **44**, 357–362. Analytical prediction of stability lobes in milling.
5. W. Kim, A. Argento and R. A. Scott 2001 *Journal of Vibration and Acoustics* **123**, 1–6. Rotating tapered composite shafts: forced torsional and extensional motions and static strength.
6. A. Tondl 1965 *Some Problems of Rotor Dynamics*. London: Chapman & Hall.
7. T. Iwatsubo 1979 *The Shock and Vibration Digest* **11**, 17–26. Stability problems on rotor systems.
8. J. Melanson and J. W. Zu 1998 *Journal of Vibration and Acoustics* **120**, 776–783. Free vibration and stability analysis of internally damped rotating shafts with general boundary conditions.
9. R. Chandra, S. P. Singh and K. Gupta 1999 *Composite Structures* **46**, 41–51. Damping studies in fiber-reinforced composites—a review.
10. Z. Hashin 1970 *International Journal of Solids and Structures* **6**, 797–807. Complex moduli of viscoelastic composites—II. Fiber reinforced materials.
11. S. Chang and C. W. Bert 1972 *Composite Materials in Engineering Design*: *Proceedings of the Sixth St. Louis Symposium* 51–62. Analysis of damping for filamentary composite materials.
12. K. Gupta and S. P. Singh 1998 *Journal of Sound and Vibration* **211**, 513–520. Damping measurements in fiber reinforced composite rotors.
13. H. Leipholz 1987 *Stability Theory*: *An Introduction to the Stability of Dynamic Systems and Rigid Bodies*, 120–135. New York: John Wiley & Sons; second edition.

14. K. M. HEAL, M. L. HANSEN and K. M. RICHARD 1996 *Maple V—Learning Guide*. New York: Springer-Verlag.
15. J. TLUSTY 1986 *Journal of Engineering for Industry* **108**, 59–67. Dynamics of high-speed milling.
16. I. MINIS and R. YANUSHEVSKY 1993 *Journal of Engineering for Industry* **115**, 1–8. A new theoretical approach for the prediction of machine tool chatter in milling.
17. J. B. DABNEY and T. L. HARMAN 1998 *Mastering Simulink* 2, NJ: Prentice-Hall.
18. L. MEIROVITCH 1970 *Methods of Analytical Dynamics*, New York: McGraw-Hill.

APPENDIX A: MONODROMY MATRIX TECHNIQUE

A short description of the monodromy matrix technique (see Meirovitch [18]) is given here. In first order form, the homogeneous equations can be written as

$$\{\dot{q}(t)\} = [B(t)]\{q(t)\}, \tag{A.1}$$

where $[B]$ is a T-periodic matrix. The system fundamental matrix is

$$[\Gamma(t)] = [\{q_1(t)\}, \{q_2(t)\}, \ldots, \{q_n(t)\}], \tag{A.2}$$

where $\{q_j(t)\}, j = 1, 2, \ldots, n$, are n linearly independent solutions. Integrating equation (A.1) n times from 0 to T with the initial conditions ($[I]$ denotes the identity matrix)

$$[\Gamma(0)] = [I], \tag{A.3}$$

numerically generates the monodromy matrix $[\Gamma(T)]$. If σ_j are the eigenvalues of $[\Gamma(T)]$, the system is stable when all the magnitudes $\|\sigma_j\| \leqslant 1$, $j = 1, \ldots, n$. The numerical integrations were done in this work by a Runge–Kutta scheme and the eigenvalue analysis was performed by MATLAB.